View metadata, citation and similar papers at core.ac.uk

brought to you by CORE

provided by St Andrews Research Repository

Effect of Halide-mixing on Tolerance Factor and Charge-carrier Dynamics in ($CH_3NH_3PbBr_{3-x}Cl_x$) Perovskites Powders

Zumaira Siddique[a,b,c], Julia L. Payne[c], John T.S. Irvine[c], Lethy K. Jagadamma[d], Zareen Akhter[a], Ifor D.W. Samuel[d], Azhar Iqbal[*a]

[a] Department of Chemistry, Quaid-i-Azam University Islamabad, 45320, Pakistan.

[b] Department of Chemistry, Government College University, New Campus Jhang Road Faisalabad, 38000, Pakistan.

[c]EastCHEM, School of Chemistry, University of St Andrews, North Haugh, St Andrews, KY16 9ST, United Kingdom.

[d]Organic Semiconductor Centre, SUPA, School of Physics and Astronomy, University of St Andrews, North Haugh, St Andrews, KY16 9SS, United Kingdom.

[*]Correspondence should be addressed to Dr. Azhar Iqbal, Email; aiqbal@qau.edu.pk

Abstract

This work demonstrates a route to making mixed halide perovskite powders at room temperature by the anti-solvent assisted crystallization method. Although, mixed halide $CH_3NH_3PbBr_{3-x}Cl_x$ perovskites have been prepared by different methods, however to best of our knowledge the anti-solvent assisted crystallization method is employed here for the first time to prepare mixed halide $CH_3NH_3PbBr_{3-x}Cl_x$ perovskites powders. Solution processed methyl ammonium lead tribromide $CH_3NH_3PbBr_3$ (x=0) and different amounts of chloride (Cl) containing mixed halide perovskites ($CH_3NH_3PbBr_{3-x}Cl_x$) were prepared for compositions of x = 0.5, 1, 1.25, 1.75. It reveals that bulk $CH_3NH_3PbBr_{3-x}Cl_x$ samples are highly crystalline and exists in pure single cubic phase with an increased tolerance factor as compared to pure $CH_3NH_3PbBr_3$. The $CH_3NH_3PbBr_3$ perovskite has space-group *Pm*-3*m* and a cell parameter of 5.930 Å (volume = 206 Å). The synthesis route adopted here gives access to hybrid perovskites powders with high Cl content and hence enables the band gap to be precisely tuned over a range from 2.26 eV to 2.49 eV. The powder samples display the subtle shifts in the emission spectra and the photoluminescence kinetics exhibits a decrease in average lifetime by increasing the Cl contents due to the presence of trap states in the structures that encourage non-radiative recombination of charge-carrier. Conventionally, the $CH_3NH_3PbBr_3$ based inverted solar cell architecture is prepared via mixing of the CH_3NH_3Br and $PbBr_2$ precursors. In contrast herein, the precursor solutions are directly prepared from the $CH_3NH_3PbBr_3$ powder and the active layer of the inverted perovskite solar cells are then spin coated using this solution. The high *Voc* value of the fabricated solar cells potentially makes it a promising candidate for tandem photovoltaic, photocatalytic water-splitting and semi-transparent photovoltaic applications.

Keywords

Perovskites; Tolerance factor; Band gap tuning; Cl incorporation; charge recombination; Photovoltaic

Graphical Abstract

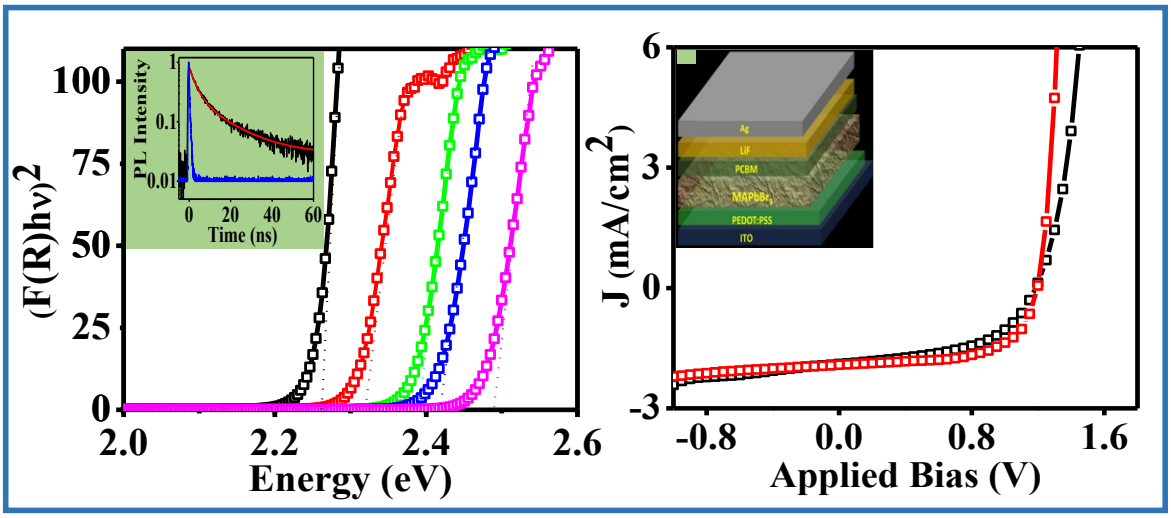

1. Introduction

Organometal halide perovskites have been widely explored as promising materials for different electro-optical devices such as light emitting diodes, solar light harvesting, optical sensors and lasers [1]. These materials have great interest because of their low manufacturing cost, fast charge generation, high absorption coefficient, easy crystallization, low recombination, long diffusion length, high charge mobility, high power conversion efficiency and tunability of optical properties [2]. High photoluminescence (PL) quantum yield, intense narrow-band PL and broad color-tunability in visible region is exhibited by different perovskites making them a suitable candidate for applications in lasers, light-emitting diodes (LEDs), photochemical

activities, electrochemical water splitting, as well as solar cells and tandem solar cells [3-8]. They have common formula of ABX_3, where A is an organic or inorganic monovalent cation ($CH_3NH_3^+$, $HC(NH_2)_2^+$, $CH_3CH_2NH_3^+$, Cs^+, Rb^+ etc.), B is an octahedrally coordinated metal cation (Pb^{2+}, Ge^{2+}, Sn^{2+}, Bi^{3+} etc.) and X is the halogen anion (Cl^-, Br^- or I^-) [9, 10]. In 2009 Miyasaka and co-workers utilized the $CH_3NH_3PbX_3$ (X= I, Br) perovskites as light sensitizers for the first time in the photovoltaic (PV) devices with ~4% efficiency and opened up the field of perovskite based solar cells as an emerging technology [11, 12]. Later on, the certified power conversion efficiency (PCE) increased remarkably and very recently, PCE above 25% has been achieved for perovskite solar cells [13-15].

The performance of perovskite materials in photovoltaic devices is critically influenced by the adopted fabrication method. Differences in the optoelectronic properties, morphology, charge carrier dynamics and crystallization can occur due to different processing methods [16]. Solvent engineering, compositional engineering, in-situ and vapour deposition techniques have been utilized for high quality perovskite materials [17-20]. Engineering of perovskite thin films may be accomplished by single step spin coating, double step consecutive deposition, vapor assisted deposition and anti-solvent assisted deposition processes [21-26]. The underlying influential factor that determines the working of the photovoltaic devices is the crystallization process of perovskite during solution deposition [27]. The anti-solvent assisted crystallization (ASAC) is a crucial choice for attaining precise solidification of perovskite materials. The solubility of a solute in solution is subsequently reduced by the addition of a secondary solvent (anti-solvent) and ultimately leads to the precipitation. Homogenous, high quality films and perovskite powders can also be obtained using this method by modulating the initial solution concentration, composition and the rate of addition of secondary solvent [28, 29].

The main purpose of the current study is to synthesize mixed halide hybrid perovskites by using the anti-solvent assisted crystallization method (ASAC). The synthesis of mixed halide $CH_3NH_3PbBr_{3-x}Cl_x$ perovskites have been reported by different methods [30, 31], however to the best of our knowledge the mixed halide $CH_3NH_3PbBr_{3-x}Cl_x$ perovskites powders are prepared for the first time by the anti-solvent assisted crystallization method. By applying this method, initially the bulk $CH_3NH_3PbBr_3$ (x=0) and then mixed halide $CH_3NH_3PbBr_{3-x}Cl_x$ (x = 0.5, 1, 1.25, 1.75) perovskite solid-state powders were prepared from their respective solution precursors. An increase of chloride content in the synthesized perovskites causes a blue-shift in the absorption and fluorescence spectra but the crystal structures of materials does not alter, suggesting that anti-solvent crystallization strategy is promising approach for the synthesis of perovskites materials with well-defined crystal structure with an enhanced tolerance factor. The band gap tuning in the UV-Vis region was attained by varying the Br to Cl weight ratios in the precursor solution. The prepared $CH_3NH_3PbBr_3$ powder was then subsequently used for the preparation of $CH_3NH_3PbBr_3$ thin films and fabrication of solar cell devices. Conventionally, $CH_3NH_3PbBr_3$ based solar cells have been prepared via the mixing of CH_3NH_3Br and $PbBr_2$ precursors. In contrast, in our present study, we prepare the precursor solutions directly from the $CH_3NH_3PbBr_3$ powder and the active layer of the inverted perovskite solar cells were then spin coated using this solution. The high V_{oc} from the fabricated solar cells and the band gap tuning in mixed halide organometal perovskites suggest multitudes of applications in optoelectronic devices.

2. Material and methods

2.1. Materials

Lead (II) bromide (98%, BDH), lead (II) chloride (98%, Sigma Aldrich), methylamine (40% wt. in H_2O, Merck), hydrobromic acid (48% in H_2O, Sigma Aldrich), absolute ethanol (99.8%), anhydrous diethyl ether (99.5%, Riedel-de Haen), toluene (99.9%, Sigma Aldrich), anhydrous N, N-dimethyl formamide (Sigma Aldrich, DMF-99.9%), di-methyl sulfoxide (Sigma Aldrich, DMSO-99.9%), gamma-butyrolactone (Sigma Aldrich, GBL-99%) and chlorobenzene anhydrous (Sigma-Aldrich, 99.8 %). All chemicals were utilized as received without any further purification.

2.2. Methyl ammonium bromide (CH_3NH_3Br) synthesis

Methyl ammonium bromide (CH_3NH_3Br) was synthesized by neutralization of pre-cooled aqueous methylamine solution (CH_3NH_2 1M, 40% in H_2O) by drop wise adding of hydrobromic acid (HBr 1M, 48% in H_2O). For complete neutralization, the mixture was constantly agitated at 0 °C for three hours in the ice bath. The white crystalline powder of CH_3NH_3Br was obtained by evaporating the solvent using rotary evaporation for one hour at 80 °C. The crystalline powder was re-dissolved in absolute ethanol and recrystallized with anhydrous diethyl ether. To obtain pure white crystalline CH_3NH_3Br, this process was repeated three times and undesired impurities were removed off. Afterwards CH_3NH_3Br crystals were also washed with diethyl ether. The crystalline white powder was collected by filtration and dried in vacuum oven for 24 hours at 80 °C. The obtained solid white colored CH_3NH_3Br product was used for the synthesis of $CH_3NH_3PbBr_3$ and other perovskite materials.

2.3. Methyl ammonium lead tribromide perovskite ($CH_3NH_3PbBr_3$) synthesis

Perovskite sensitizer solution of $CH_3NH_3PbBr_3$ was prepared by mixing stoichiometric amount of lead bromide ($PbBr_2$ 1.84 g, 0.5 M) and the synthesized methyl ammonium bromide (CH_3NH_3Br, 0.56 g, 0.5 M) powder in the high boiling point DMF solvent. The resultant solution was continuously stirred at 60 °C for 24 hours. The $CH_3NH_3PbBr_3$ powder was prepared through precipitation by using the anti-solvent toluene at room temperature. The orange colored $CH_3NH_3PbBr_3$ powder was obtained by rapidly injecting 1 mL of $CH_3NH_3PbBr_3$ solution in 5 mL of stirring toluene. After centrifugation at 4000 rpm for 120 seconds the supernatant was discarded and residue of $CH_3NH_3PbBr_3$ was oven dried for 24 hours at 80 °C.

2.4. Mixed halide perovskites ($CH_3NH_3PbBr_{3-x}Cl_x$) synthesis

Chloride containing mixed halide $CH_3NH_3PbBr_{3-x}Cl_x$ perovskite solutions (0.5 M) were prepared in 10 mL DMF. The x values 0.5, 1.0, 1.25 and 1.75 corresponds to the weight ratio compositions: $CH_3NH_3PbBr_{2.5}Cl_{0.5}$, $CH_3NH_3PbBr_2Cl_1$, $CH_3NH_3PbBr_{1.75}Cl_{1.25}$ and $CH_3NH_3PbBr_{1.25}Cl_{1.75}$, respectively. For x=0.5 $CH_3NH_3PbBr_{2.5}Cl_{0.5}$ perovskite 0.6 g CH_3NH_3Br, 1.54 g $PbBr_2$ and 0.31 g $PbCl_2$ were added and stirred continuously in DMF for 24 hours at 60 °C. Similarly, other compositions were also prepared by adding 0.6 g CH_3NH_3Br, 1.23 g $PbBr_2$ and 0.62 g $PbCl_2$ (x=1), 0.6 g CH_3NH_3Br, 1.1 g $PbBr_2$ and 0.77 g $PbCl_2$ (x=1.25) and 0.6 g CH_3NH_3Br, 0.77 g $PbBr_2$ and 1.1 g $PbCl_2$ (x=1.75) in 10 mL DMF. The solidification of mixed halide powders was achieved by using toluene as anti-solvent. 1 mL of mixed halide solution was added in 5 mL of stirred toluene in separate vials to obtain different mixed halide precipitates. After centrifugation at 4000 rpm for 120 seconds, the supernatants were discarded and residues were dried in vacuum oven for 24 hours at 80 °C, which gave the desired products.

2.5. Characterization techniques

The surface morphology of 3-D $CH_3NH_3PbBr_3$ and $CH_3NH_3PbBr_{3-x}Cl_x$ perovskites was studied by field emission scanning electron microscopy (FESEM, MIRA 3 XMU coupled energy dispersive X-ray, EDX). A PerkinElmer Lambda 35 UV-Vis spectrometer was used at room temperature to measure the reflectance spectrum of the powder samples. Flau Time 300 (FT-300) steady-state and lifetime spectrometer, Pico Quant GmbH Germany, was used to study the fluorescence spectra and kinetics. The samples films were excited at 306 nm with a pulsed PLS-300 LED excitation source and the photoluminescence (PL) spectra and kinetics of the synthesized perovskite materials were collected under ambient conditions as described previously [32, 33]. Powder X-ray diffraction (XRD) analysis was performed with a PANalytical X'Pert Pro diffractometer by using Cu $K\alpha_1$ radiation in the 2θ range of 10-70° at room temperature. A METTLER TOLEDO TGA-1 thermogravimetric analyzer was used to investigate thermal stability of $CH_3NH_3PbBr_3$ sample (28.04 mg) in Al_2O_3 crucible, heated from room temperature to 1000 ºC under nitrogen atmosphere. The heating rate and gas flow rate were 10 ºC/minute and 50 mL/minute, respectively. TGA/HT DSC HSS2 sensor was used for differential scanning calorimetry (DSC) analysis at the ramping rate of 10 ºC/minute in nitrogen environment.

2.6. Solar cell device fabrication

As reported earlier, the use of mixed solvents in the device fabrication of perovskite solar cells has increased the compactness of the films. Mixed solvents help to achieve higher surface coverage with the formation of smooth and uniform films of perovskites when compared to individual solvents [34, 35]. In this regard, a mixed solvent consisting of GBL and DMSO in the 7:3 v/v % ratio was used to prepare $CH_3NH_3PbBr_3$ active layer solution in our fabricated solar

cell devices. The concentration of the prepared solution is 200 mg /mL. The precursor solution was stirred overnight (~ 17 hours) at 60 °C inside N_2 filled glove box. Indium tin oxide (ITO) coated glass substrates (2 × 2 cm^2) were employed to fabricate the perovskite solar cells. Substrates were cleaned before the deposition of the different functional layers. Detergent, deionized water, acetone and 2-propanol were consecutively engaged in ultra-sonication bath for the cleaning of ITO-coated glass substrates, followed by drying in N_2 stream. To remove organic residues from the substrate surface and to improve the wettability, the substrates were plasma-cleaned for a duration of 3 minutes. Thin films of PEDOT:PSS (Clevios- VP AI 4083) aqueous solution were prepared on the ITO glass substrates by spin coating for 60 seconds at 4000 rpm and dried on a hot plate for 20 minutes at 130 °C. These films were then transferred into a N_2 filled glove box. The perovskite active solution was filtered through a 0.2 μm PTFE filter, before spin coating onto the ITO/PEDOT:PSS substrate. The two-step spin coating condition was 1000 rpm for 10 seconds and 4000 rpm for 40 seconds. After 20 seconds of the second step, 300 μL of toluene was added on to the spinning substrate. Then the substrates were annealed for 10 minutes at 100 °C. The $PC_{60}BM$ (American Dye Sources) electron transporting layer was prepared from a 10 mg/mL chlorobenzene solution (filtered with a 0.2 μm PTFE pores) and spin coated at 1000 rpm for 60 seconds. The LiF (1 nm)/Ag (100 nm) electrode was deposited by thermal evaporator at a pressure of 10^{-6} mbar. The active area of the solar cell device was 3 mm × 2 mm. The final device architecture was Glass/ITO/PEDOT:PSS/$CH_3NH_3PbBr_3$/PCBM/LiF/Ag. Afterwards, the solar cells were encapsulated by UV-epoxy and measured under 1 sun illumination by Sciencetech solar simulator. The illumination intensity was verified by using a calibrated mono silicon detector and a KG-5 filter. The external quantum efficiency (EQE) measurements were performed at zero bias

by illuminating the device with monochromatic light supplied from a Xenon arc lamp in combination with a Bentham TMc300 monochromator.

3. Results and discussion

The modified Goldschmidt's tolerance factor ($t_{effective}$) is employed to predict the stable ABX_3 cubic crystal structure of perovskite materials. The effective anionic radius (r anion), effective tolerance factor ($t_{effective}$) and octahedral factor (μ) is estimated by following equations:

$$(r\ anion)_{(effective)} = xCl^{-1} + (1-x)Br^{-1} \quad (1)$$

$$t_{(effective)} = \frac{[(r\ CH3NH3^{+1}) + (r\ anion_{(effective)})]}{\sqrt{2}\,[(r_{Pb^{+2}}) + (r\ anion_{(effective)})]} \quad (2)$$

$$u = \frac{r\ Pb^{+2}}{r\ anion_{(effective)}} \quad (3)$$

The ionic radii of $CH_3NH_3^+$, Pb^{2+}, Br^- and Cl^- are 2.17 Å, 1.19 Å, 1.96 Å and 1.81 Å, respectively [36]. Ideal cubic perovskite configuration occurs when the ($t_{effective}$) value for perovskite is in the range of 0.80 - 1.0 and octahedral factor (μ) should be over 0.40 [37, 38]. Below 0.8 or above 1.0, orthorhombic and hexagonal configurations tend to form by perovskites. If the value of tolerance factor is 1 or smaller than 0.7 then non-perovskite structures are predominantly observed [39]. The calculated results for tuning the tolerance factor by mixed halide $CH_3NH_3PbBr_{3-x}Cl_x$ (x = 0.5, 1, 1.25, 1.75) perovskites are shown in Table 1. The tolerance factor of mixed halide perovskites (0.933-0.947) is enhanced as compare to pure $CH_3NH_3PbBr_3$ (0.927) which suggests that with the substitution of more electronegative chloride contents (small sized) in place of less electronegative bromide (large sized), the cubic structural configuration in mixed halide perovskites gains more stability and moves toward more ideal cubic structure formation.

Table 1. The effective anionic radius (r anion), effective tolerance factor ($t_{effective}$) and octahedral factor (μ) for $CH_3NH_3PbBr_3$ (x=0), $CH_3NH_3PbBr_{2.5}Cl_{0.5}$ (x=0.5), $CH_3NH_3PbBr_2Cl_1$ (x=1), $CH_3NH_3PbBr_{1.75}Cl_{1.25}$ (x=1.25) and $CH_3NH_3PbBr_{1.25}Cl_{1.75}$ (x=1.75) perovskites.

Compound	**X values**	**(r anion)$_{effective}$ (Å)**	**Effective tolerance factor ($t_{effective}$)**	**Octahedral factor (μ)**
$CH_3NH_3PbBr_3$	0	1.960	0.927	0.607
$CH_3NH_3PbBr_{2.5}Cl_{0.5}$	0.5	1.885	0.933	0.631
$CH_3NH_3PbBr_2Cl_1$	1	1.810	0.938	0.658
$CH_3NH_3PbBr_{1.75}Cl_{1.25}$	1.25	1.773	0.941	0.671
$CH_3NH_3PbBr_{1.25}Cl_{1.75}$	1.75	1.698	0.947	0.701

In order to understand the phase purity and crystal structures of $CH_3NH_3PbBr_{3-x}Cl_x$ perovskites, powder XRD analysis was conducted. **Figure 1 (a)** displays the XRD pattern of synthesized $CH_3NH_3PbBr_3$ perovskite material (black trace). The sharp peaks in XRD patterns of $CH_3NH_3PbBr_3$ demonstrate that the sample is highly crystalline, and also no impurity peak is observed which confirms its phase purity. The diffraction data can be indexed to space-group *Pm*-3*m* and a cell parameter of 5.930 Å with volume = 206 Å, which is in good agreement with the published structural model of $CH_3NH_3PbBr_3$ [40-42]. All peaks in all XRD patterns of $CH_3NH_3PbBr_{2.5}Cl_{0.5}$ (x=0.5), $CH_3NH_3PbBr_2Cl_1$ (x=1), $CH_3NH_3PbBr_{1.75}Cl_{1.25}$ (x=1.25) and $CH_3NH_3PbBr_{1.25}Cl_{1.75}$ (x=1.75) perovskite powders can be accounted for in space group *Pm*-3*m,*

with a cubic unit cell parameter ranging from ~5.93 Å to 5.84 Å, indicating that all samples are pure. No impurity peaks are observed in any of the diffraction patterns. **Figure 1 (b)** represents the unit cell parameters of mixed halide perovskites whose value decreased with the increase in the amount of chloride component in the perovskite structures due to the substitution of smaller chloride atom instead of larger bromide atom in perovskites [43]. The Miller indices for all peaks in the diffraction patterns of the powdered samples are given in the Table S1. Based on the EDX and XRD results, it is deduced that $CH_3NH_3PbBr_{3-x}Cl_x$ perovskite crystals are present in phase pure cubic materials. Similarly, the thin film diffraction pattern of $CH_3NH_3PbBr_3$ used in solar cell device preparation can be assigned to a phase pure sample. All peaks can be indexed to a cubic unit cell with a = 5.9274(12) Å. The diffraction patterns of thin film correspond to the (100), (200), (300) and (400) miller indices, designating that basic perovskite cubic structure remain unchanged Figure S1.

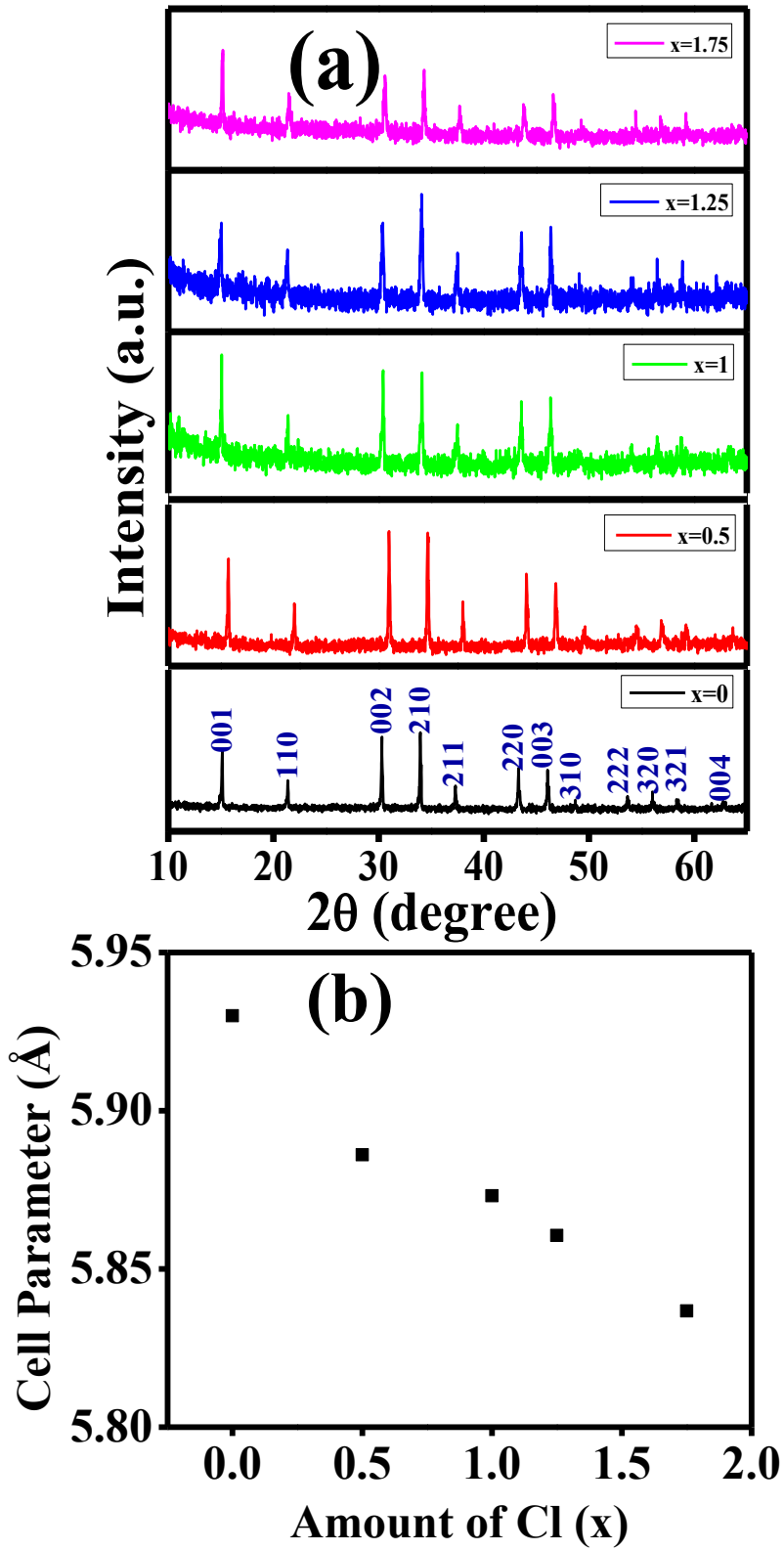
(a)
x=1.75
x=1.25
x=1
x=0.5
x=0
Intensity (a.u.)
001
110
002
210
211
220
003
310
222
320
321
004
10
20
30
40
50
60
2θ (degree)
(b)
Cell Parameter (Å)
5.95
5.90
5.85
5.80
0.0
0.5
1.0
1.5
2.0
Amount of Cl (x)

Figure 1. (a) XRD patterns of mixed halide perovskite powder samples, (b) calculated unit cell parameters of $CH_3NH_3PbBr_3$ (x=0), $CH_3NH_3PbBr_{2.5}Cl_{0.5}$ (x=0.5), $CH_3NH_3PbBr_2Cl_1$ (x=1), $CH_3NH_3PbBr_{1.75}Cl_{1.25}$ (x=1.25) and $CH_3NH_3PbBr_{1.25}Cl_{1.75}$ (x=1.75) perovskites.

The morphology and chemical composition of mixed halide perovskites were analyzed by scanning electron microscopy (SEM) and energy dispersive X-ray (EDX) analysis, respectively. The SEM micrograph of synthesized $CH_3NH_3PbBr_3$ perovskite powder (x=0) is shown in **Figure 2 (a)**, which demonstrates that the $CH_3NH_3PbBr_3$ is present in the form of cuboidal microcrystals. The typical size of cubic crystal particles was ≈ 1 μm. The $CH_3NH_3PbBr_3$ perovskites microcrystals of size 1-100 μm were also prepared by employing vapor-assisted solution process at room temperature [44]. The SEM micrographs of mixed halide perovskites are displayed in **Figure 2 (b-e)**, which reveals that the synthesized materials exist in the form of cuboidal microcrystals of different sizes. The slight variation in morphology of Cl substituted perovskites may be related to the small size of Cl ions (1.81 Å) as compare to larger Br ions (1.96 Å). With the substitution of Cl ions for Br ones, some sort of strain is produced on the anion site in the lattice structure, which probably leads to a little change in perovskite lattice with the production of different defects in structure. The full width at half maximum (FWHM) of 002 XRD peak of mixed halide perovskite is increased from 0.147-0.22° (Table S2) which would be expected due to smaller crystallite size and strain effects due to Cl and Br occupying the same site in the crystal structure in these mixed halide perovskite materials. Different strategies have been employed and their corresponding effects on the crystallinity and surface morphology of perovskite materials have been discussed in detail in literature [45-47]. The atomic composition of mixed halide perovskites ($CH_3NH_3Br_{3-x}Cl_x$) are shown in **Table 2** and

their corresponding EDX spectra as displayed in **Figure S2**. It is demonstrated that 3:1 atomic % of Br/Pb was present in $CH_3NH_3PbBr_3$ (x=0). As the amount of chloride component is increased, the bromide concentration decreased in the synthesized mixed halide perovskites. The EDX spectra display no impurity peaks and the atomic % ratios of Pb, Br and Cl are in good agreement with the expected ratios of these components in mixed halide perovskite, which provide evidence for the successful synthesis of different perovskite materials by the anti-solvent assisted crystallization method.

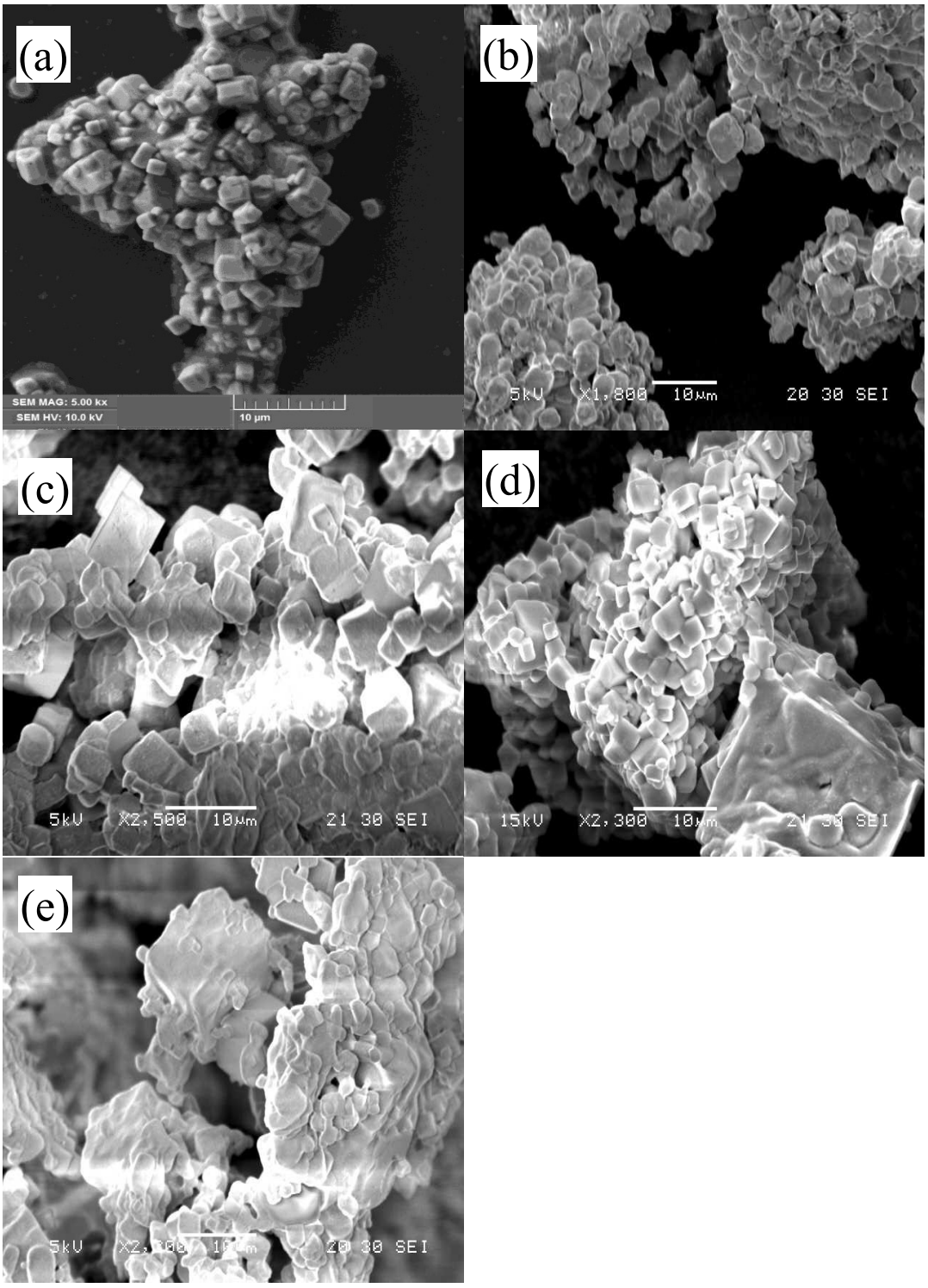

Figure 2. SEM micrographs of (a) $CH_3NH_3PbBr_3$ powder (x=0), (b) $CH_3NH_3PbBr_{2.5}Cl_{0.5}$ (x=0.5), (c) $CH_3NH_3PbBr_2Cl_1$ (x=1), (d) $CH_3NH_3PbBr_{1.75}Cl_{1.25}$ (x=1.25) and (e) $CH_3NH_3PbBr_{1.25}Cl_{1.75}$ (x=1.75) perovskites.

Table 2. Chemical constituents present in mixed halide perovskites ($CH_3NH_3PbBr_{3-x}Cl_x$) assessed from EDX analysis.

Compound	Weight %			Atomic %			Total
	Element			Element			
	Cl K	Br L	Pb M	Cl K	Br L	Pb M	
$CH_3NH_3PbBr_3$ (X=0)	-	55.0	45.0	-	74.7	25.3	100
$CH_3NH_3PbBr_{2.5}Cl_{0.5}$ (X=0.5)	3.7	45.6	50.7	11.4	62.0	26.6	100
$CH_3NH_3PbBr_2Cl_1$ (X=1)	10.2	41.5	48.3	27.6	50.0	22.4	100
$CH_3NH_3PbBr_{1.75}Cl_{1.25}$ (X=1.25)	13.1	37.2	49.7	34.4	43.3	22.3	100
$CH_3NH_3PbBr_{1.25}Cl_{1.75}$ (X=1.75)	15.5	28.5	56.0	41.0	33.6	25.4	100

The UV-Vis reflectance spectrum of powder $CH_3NH_3PbBr_3$ (x=0) and the corresponding mixed halides are shown in **Figure 3 (a)**. In the case of $CH_3NH_3PbBr_3$ powder, there is a sudden decrease in reflectance at 580 nm and this sharp decrease in the reflectance provides an evidence of direct band gap material. **Figure 3 (a)** shows that, the UV-Vis reflectance spectra of $CH_3NH_3PbBr_{3-x}Cl_x$ (x=0, 0.5, 1, 1.25, 1.75) powders are blue-shifted in comparison to $CH_3NH_3PbBr_3$ with an increase in the amount of chloride component. The optical band gaps (E_g) of $CH_3NH_3PbBr_{3-x}Cl_x$ (x=0, 0.5, 1, 1.25, 1.75) powders are estimated by the Kubelka−Munk equation [48] (eq. 4) and are found to be in the visible region of the spectrum.

$$F(R) = (1 - R)^2/2R \qquad [F(R)h\nu]^2 = A(h\nu - E_g) \quad (4)$$

The Kubelka−Munk function F(R) is associated with the absorption coefficient (α) of the material and R represent the absolute reflectance, A is a constant, *hv* is photon energy and E_g represents the band gap of the material. By extrapolating the linear part of $[F(R)\ h\nu]^2$ *vs* photon energy (eV) to zero of y-axis we estimated the band gaps of these materials as displayed by **Figure 3 (b)**. The optical band gaps of mixed halide perovskites $CH_3NH_3PbBr_{3-x}Cl_x$ were varied from 2.26 to 2.49 eV by increasing the incorporation of chloride content from x=0 to x= 1.75. This unremitting blue shift in absorption and higher band gaps in mixed halide perovskites is attributed to the change in the interaction of orbitals from bromide (Br-4p) to chloride (Cl-5p) participating in bond formation with Pb ions (6p). The estimated band gap values match with the previously reported band gap of mixed bromide/chloride, $CH_3NH_3PbBr_{3-x}Cl_x$ system with comparable x-values [49].

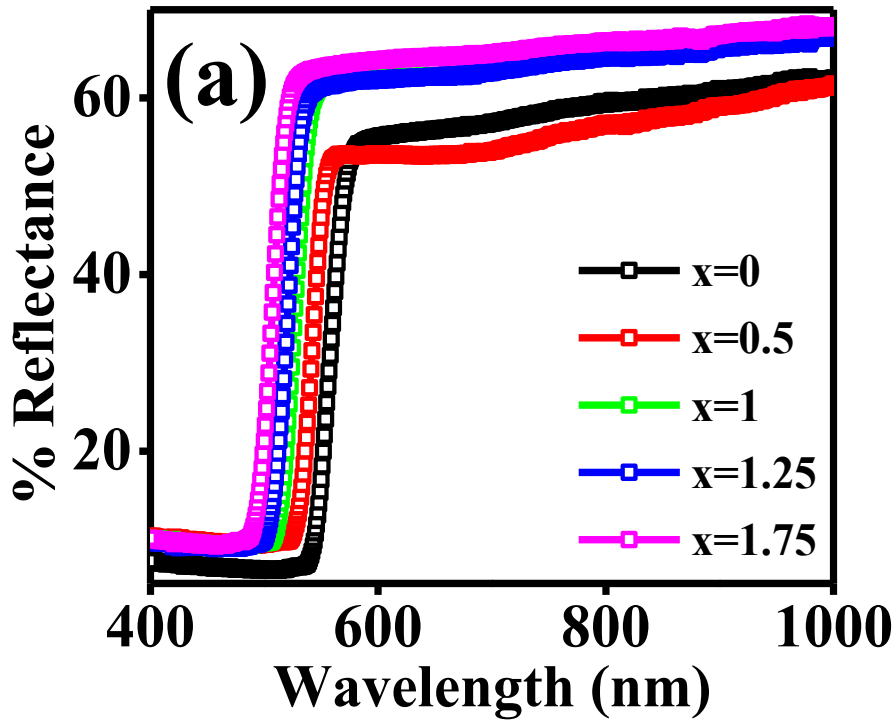
(a)
% Reflectance
60
40
20
400
600
800
1000
Wavelength (nm)
x=0
x=0.5
x=1
x=1.25
x=1.75

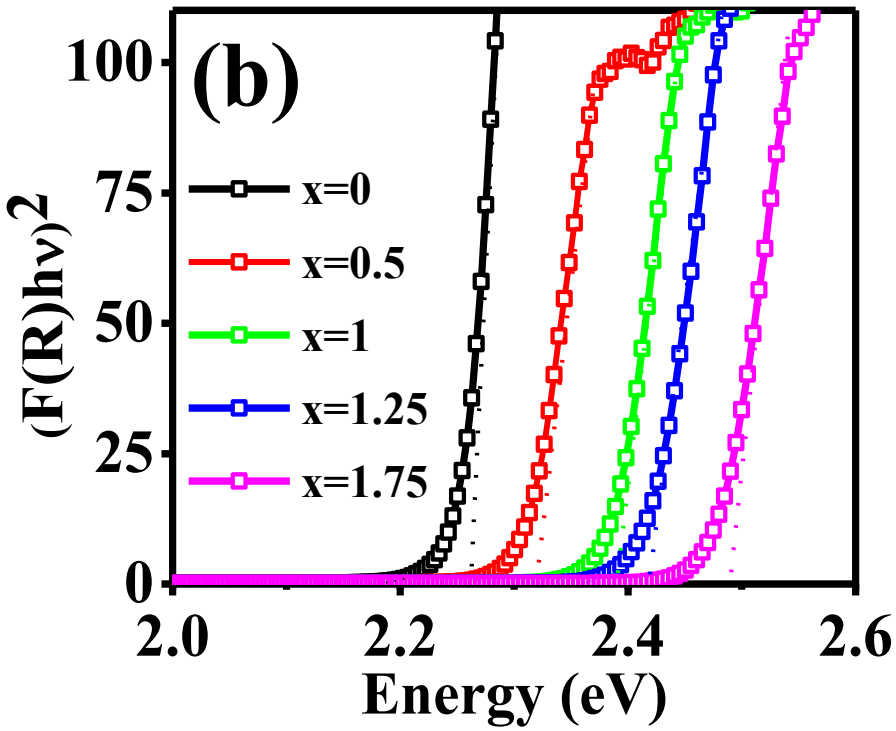
(b)
(F(R)hν)2
100
75
50
25
0
2.0
2.2
2.4
2.6
Energy (eV)
x=0
x=0.5
x=1
x=1.25
x=1.75

Figure 3. (a) UV–Vis reflectance spectra, (b) optical band gaps estimation of $CH_3NH_3PbBr_3$ (x=0), $CH_3NH_3PbBr_{2.5}Cl_{0.5}$ (x=0.5), $CH_3NH_3PbBr_2Cl_1$ (x=1), $CH_3NH_3PbBr_{1.75}Cl_{1.25}$ (x=1.25) and $CH_3NH_3PbBr_{1.25}Cl_{1.75}$ (x=1.75) perovskite powders.

A thick paste of $CH_3NH_3PbBr_3$ (x=0) was prepared in methanol and deposited on a clean glass slide to measure its steady-state photoluminescence (SSPL) spectrum. It exhibited a broad emission peak at 550 nm (2.25 eV) as shown in **Figure 4 (a)**. The emission peak can be assigned to the direct recombination of photo-generated charge-carrier. The small hump around 435 nm may be due to light scattering by the solvent molecules or due to the existence of $PbBr_6$ whose presence is so small, that it does not show any feature in XRD analysis owing to beyond the detection limit of the XRD. The SSPL spectra of $CH_3NH_3PbBr_{3-x}Cl_x$ (x=0, 0.5, 1, 1.25, 1.75) perovskites, **Figure 4 (a)**, display a blue-shift of 0.11 eV from 550 nm (2.25 eV) to 525 nm (2.36 eV) from the parent $CH_3NH_3PbBr_3$ (x=0) PL spectrum. This blue-shift is attributed to the accommodation of chloride components in these perovskite materials that lead to increase in the band gap.

Time-resolved photoluminescence measurements (TRPL) were conducted to understand the photo-injected charge-carrier dynamics of the prepared samples. The PL decay kinetics of $CH_3NH_3PbBr_3$ (x=0) are displayed in **Figure 4 (b)** and the measured PL kinetics are best fitted by a combination of two unimolecular recombination kinetics models (bi exponential decay function) [50-52] as displayed by equation (5).

$$A(t) = A_1 \exp(-t/\tau_1) + A_2 \exp(-t/\tau_2) \qquad (5)$$

Here A_1, A_2, are the associated coefficients (pre-exponential factors) and τ_1 and τ_2 are the time constants of each component, respectively. The extracted parameters from the best fit are given

in **Table S3**. The measured PL kinetics of $CH_3NH_3PbBr_3$ (x=0) at 547 nm suggests the PL mainly decays by trap assisted recombination originating from two distinct channels, represented by two time constants, τ_1 = 3.3 ns (69 %) and τ_2 =15.4 ns (31 %). As suggested by the pre-exponential factor A_1, the 69 % of PL is decayed in 3.3 ns, suggesting the photo-generated charge-carrier are readily trapped in the trap states. The long lifetime component, τ_2 =15.4 ns suggests almost 31% of photo-injected charge-carrier (electrons and holes) recombine directly from conduction band to valence band [53]. It has also has been reported the PL kinetics of $CsPbBr_3$ single crystal exhibits time constants of τ_1 = 23 ns and τ_2 =233 ns that are related to the surface and bulk carrier recombination [54]. As previously discussed by FWHM values that with the chloride substitution, more trap states are introduced in the structures, which are expected to lead toward the shortening of PL lifetime in mixed halide perovskite materials. However, this shortening of lifetime is not visible in **Figure 4 (c)** due to the limited instrument response (0.5 ns) of our TCSPC setup. The attempts to fit the PL data with a bi-molecular recombination model was also made but none of the data was adequately fitted with this model. The best fits obtained by combination of two unimolecular decay kinetics model suggesting majority of charge-carrier recombine non-radiatively through the trap states. The amplitude weighted $\tau_{average}$ of charge-carrier is estimated by equation (6) and the values are presented in **Table S3**.

$$\tau_{average} = \frac{A_1\tau_1 + A_2\tau_2}{A_1 + A_2} \qquad (6)$$

The calculated average radiative lifetime ($\tau_{average}$) of $CH_3NH_3PbBr_3$ (x=0) is 7.07 ns and with chloride substitution its value is decreased. The $\tau_{average}$ values of $CH_3NH_3PbBr_{2.5}Cl_{0.5}$ (x=0.5), $CH_3NH_3PbBr_2Cl_1$ (x=1), $CH_3NH_3PbBr_{1.75}Cl_{1.25}$ (x=1.25) and $CH_3NH_3PbBr_{1.25}Cl_{1.75}$ (x=1.75) are 4.80, 5.42, 5.82 and 5.98 ns, respectively. This type of faster PL decay behavior is also observed in $CsPb(Br/Cl)_3$ perovskite nanocrystals, in which $\tau_{average}$ decreased with the increase in higher

band gap causing Cl component in the structure [55]. The possible fates of photo-induced charge-carrier recombination dynamics are explained by a simple pictorial diagram presented in **Figure 4 (d)**.

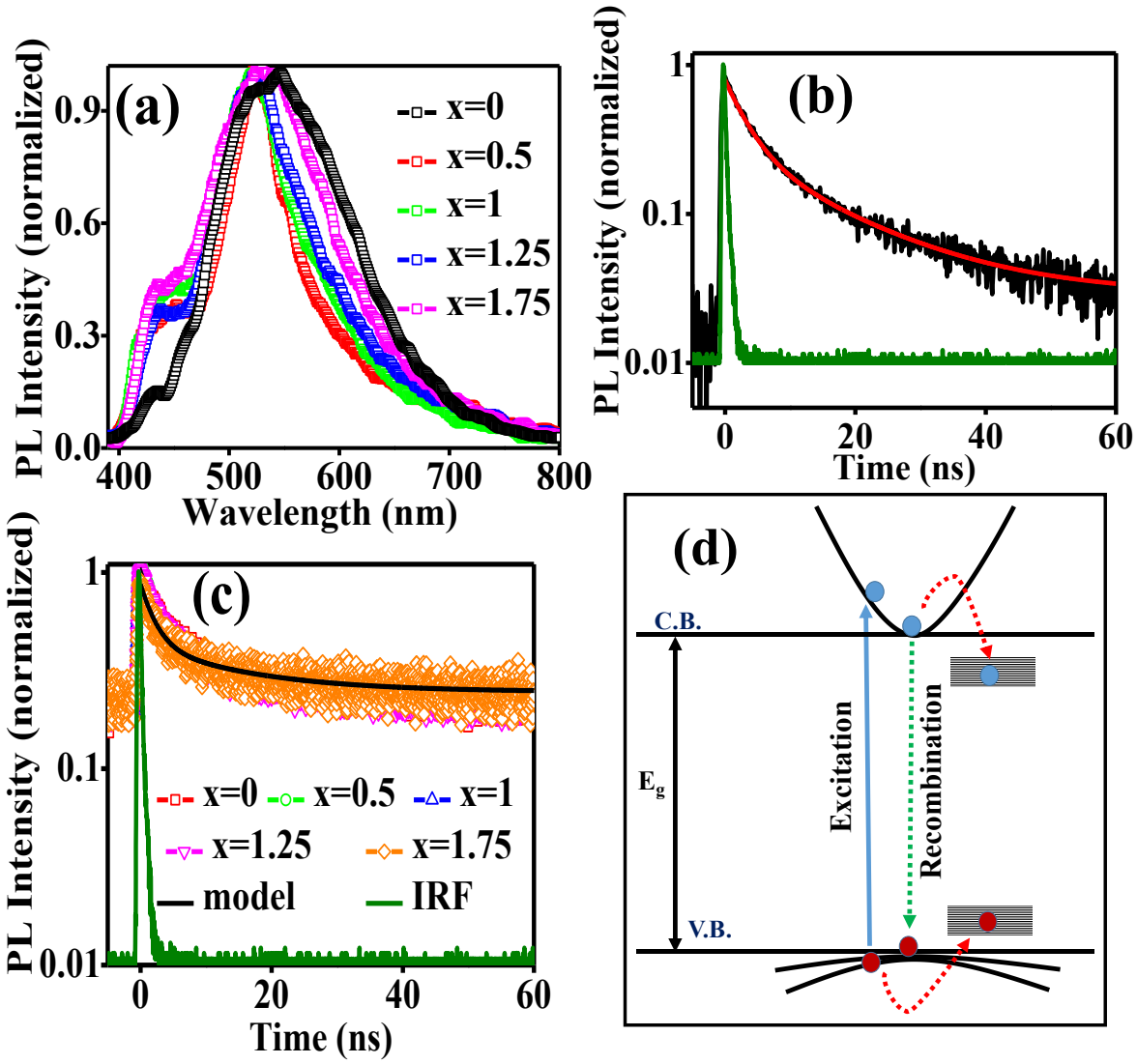

Figure 4. (a) SSPL spectra of $CH_3NH_3PbBr_{3-x}Cl_x$ powders (λ_{exc} ~ 306 nm pulse laser), (b) PL decay kinetics (black trace), model fit (red trace) and IRF (olive trace) of $CH_3NH_3PbBr_3$ (x=0), (c) PL decay kinetics trace of $CH_3NH_3PbBr_3$ (x=0), $CH_3NH_3PbBr_{2.5}Cl_{0.5}$ (x=0.5,

$CH_3NH_3PbBr_2Cl_1$ (x=1), $CH_3NH_3PbBr_{1.75}Cl_{1.25}$ (x=1.25) and $CH_3NH_3PbBr_{1.25}Cl_{1.75}$ (x=1.75) perovskites and (d) recombination fates of photo-generated charge-carriers.

The thermal stability of $CH_3NH_3PbBr_3$ (x=0) was evaluated by thermo-gravimetric analysis (TGA). As indicated in **Figure S3 (a)** the synthesized $CH_3NH_3PbBr_3$ perovskite was thermally stable up to 254 °C. The sample decomposed in two major steps upon heating up to 1000 °C. **Table S4** showed the peak temperatures (T_p) of TG / DTG thermograms. The decomposition above 254 °C was attributed to the removal of CH_3NH_3Br, which lead to the weight loss of 23 % at 430 °C. It may be related to the liberation of CH_3NH_3Br or its decomposition into methylamine and HBr. As the temperature increased from 450 °C to 642 °C, further weight loss of 70 % could be ascribed to the thermal decomposition of the inorganic part $PbBr_2$ and melting of the perovskite material. This type of thermal behavior is in accordance with the findings of Biwu *et al*., [56].

Differential scanning calorimetry (DSC) analysis showed a distinct feature in DSC curve of the synthesized methyl ammonium lead bromide ($CH_3NH_3PbBr_3$) perovskite at 375 °C, which represented the melting temperature of lead bromide ($PbBr_2$), as shown in **Figure S3 (b)**. Complete decomposition of perovskite material was observed with further increase in temperature. Similar thermal behavior has been observed for other perovskite materials used in solar cell devices [57].

After the structural and optical characterization of the synthesized $CH_3NH_3PbBr_3$ (x=0) perovskite powder, it was investigated for photovoltaic application. The $CH_3NH_3PbBr_3$ thin films were prepared as described in the experimental section and their UV-Vis absorption spectrum of the prepared thin film is displayed in **Figure 5 (a)** suggesting the first excitonic absorption at

~550 nm. The J-V characteristics of the prepared solar cell device under 1 Sun illumination are presented in **Figure 5 (b)** and the solar cell performance parameters are listed in **Table 3**. The maximum power conversion efficiency obtained is 1.4 %. As displayed in **Table 3**, the main factor that limits the photovoltaic performance is the short circuit current density (J_{sc}). This can be attributed to the wide band gap of the $CH_3NH_3PbBr_3$ thin film and the less absorption of the solar spectrum in visible and near IR region. This is further revealed in the external quantum efficiency (EQE) spectrum as shown in **Figure 5 (c)**. The inverted device architecture used for the solar cell fabrication is shown in **Figure 5 (d)**. The V_{oc} of the solar cells is high and is ~1.2 V. The photovoltaic performance for $CH_3NH_3PbBr_3$ is poor than the previously reported PCEs of ~ 2-5% [58-60]. This could be related to the starting precursor being different, e.g., $CH_3NH_3PbBr_3$ vs (CH_3NH_3Br + $PbBr_2$) and not-fully optimized solar cell device parameters (such as active layer thickness, use of efficient counter electrodes, solvent and interface engineering) [61]. Table S5 also represent power conversion efficiencies of $CH_3NH_3PbBr_3$ perovskites in comparison to $CH_3NH_3PbBr_3$ based solar cells prepared in this work. The efficiency of perovskites could be improved by manipulating different practices such as interface engineering by using different organic material or small molecular additives which absorb light in NIR region [62-66]. The $CH_3NH_3PbBr_3$ thin film was selected for photovoltaic applications since the chloride based mixed halides have higher band gap compared to $CH_3NH_3PbBr_3$ as shown in **Figure 3 (b)**. As reported earlier, with the controlled tuning of band gaps to higher values these mixed halide perovskite materials could be utilized to prepare semi-transparent or transparent UV light harvesting photovoltaic devices [67]. Even though the spectral overlap of the absorption spectrum of $CH_3NH_3PbBr_3$ with the visible solar spectral region is poor, resulting in low power conversion efficiency, their semi-transparent nature and better overlap with the indoor light

spectral region such as white LEDs, makes it a promising candidate for tandem solar cells, indoor solar cells and semi-transparent photovoltaic devices.

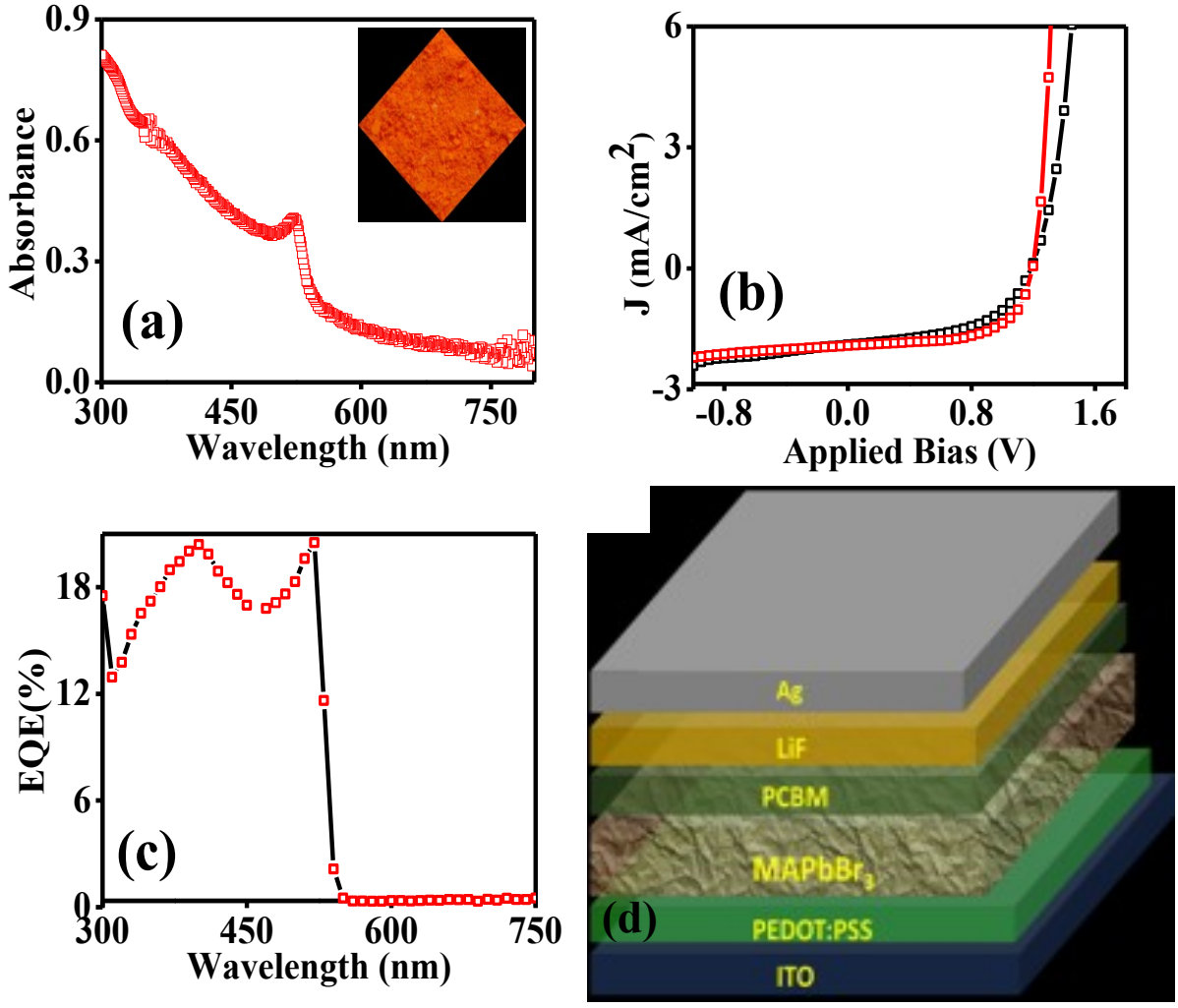

Figure 5. (a) UV-Vis absorption spectrum of the $CH_3NH_3PbBr_3$ thin film, inset showed the orange colored photograph of $CH_3NH_3PbBr_3$ powder, (b) J-V characteristics (forward scan-black line and reverse scan-red line), (c) EQE spectrum of the fabricated $CH_3NH_3PbBr_3$ solar cell and (d) inverted device architecture used for the fabrication of $CH_3NH_3PbBr_3$ solar cells.

Table 3. Inverted solar cell performance parameters for $CH_3NH_3PbBr_3$ based solar cells. The solar cell performance parameters are averaged over 7 devices and ± values show the standard deviation. (FW-forward scan and RW–reverse scan).

Scan	***Jsc*** **(mA/cm^2)**	***Voc*** **(V)**	**FF (%)**	**Rsh (ohm cm^2)**	**Rs (ohm cm^2)**	**PCE (%) average**	**PCE (%) best**
FW	1.70±0.35	1.17±0.03	53.8±3.6	3342±1314	2.74±0.53	1.07±0.18	1.17
RW	1.57±0.48	1.18±0.03	58.4±6.3	6034±2736	4.73±2.15	1.08±0.36	1.41

4. Conclusions

This study clearly demonstrated that the anti-solvent crystallization method adopted here was an easy approach to prepare the solid powder of mixed halide perovskites. The powder XRD analysis revealed that the $CH_3NH_3PbBr_{3-x}Cl_x$ samples were highly crystalline and had cubic symmetry, and exhibited an enhanced tolerance factor. FESEM showed that the samples were in the form of bulk cubes. The UV-Vis reflectance and PL spectra of mixed perovskites were blue-shifted by increasing the chloride content in $CH_3NH_3PbBr_{3-x}Cl_x$ perovskites. By changing the chloride contents, the band gap of the mixed halide perovskites was varied from 2.26 eV to 2.49 eV. The PL kinetics measurements demonstrated that the major part of the photo-injected charge-carrier recombine non-radiatively by recombination through the trap states with average radiative lifetimes of 7.07 ns (for x = 0) to 4.80 ns (for x = 0.5). Due to the limited instrument response function the fast trapping of charge-carrier was not convincingly visible in our measurements. The thermal studies demonstrated that $CH_3NH_3PbBr_3$ was stable at room

temperature and started to degrade at 250℃. The 2.26 eV direct optical band gap of $CH_3NH_3PbBr_3$ and high V_{oc} (1.2 eV) makes it a highly suitable candidate for low cost tandem solar cells, indoor solar cells and semi-transparent photovoltaic devices.

5. Acknowledgements

The authors are highly thankful for the financial support of Higher Education Commission (HEC) Pakistan through the equipment/research grants (6976/Federal/NRPU/R&D/HEC/2017), (20-3071/NRPU/R&D/HEC/13). Author ZS acknowledges HEC for indigenous PhD Fellowship Phase-II, Batch-II, 2013, PIN 213-66018-2PS2-127 and International Research Support Initiative Programme (IRSIP). Author LKJ acknowledges support from a Marie Skłodowska-Curie Individual Fellowship (European Commission) (MCIF: No. 745776).

References

1. H. Huang, F. Zhao, L. Liu, F. Zhang, X. G. Wu, L. Shi, B. Zou, Q. Pei, H. Zhong, Emulsion synthesis of size-tunable $CH_3NH_3PbBr_3$ quantum dots: an alternative route toward efficient light-emitting diodes. ACS Appl. Mater. Interfaces **7**, 28128-28133 (2015)
2. K. Zheng, K. Zidek, M. Abdellah, M.E. Messing, M.J.A. Marri, T.N. Pullerits, Trap states and their dynamics in organometal halide perovskite nanoparticles and bulk crystals. J. Phys. Chem. C **120**, 3077-3084 (2016)
3. D.M. Jang, K. Park, D. H. Kim, J. Park, F. Shojaei, H. S. Kang, J. P. Ahn, J. W. Lee, J. K. Song, Reversible halide exchange reaction of organometal trihalide perovskite colloidal nanocrystals for full-range band gap tuning. Nano Lett. **15**, 5191-5199 (2015)
4. A. Mojiri, R. Taylor, E. Thomsen, G. Rosengarten, Spectral beam splitting for efficient conversion of solar energy-A review. Renew. Sust. Energy Rev. **28**, 654-663 (2013)
5. N. Kedem, T.M. Brenner, M. Kulbak, N. Schaefer, S. Levcenko, I. Levine, D. A. Ras, G. Hodes, D. Cahen, Light-induced increase of electron diffusion length in a p–n junction type $CH_3NH_3PbBr_3$ perovskite solar cell. J. Phys. Chem. Lett. **6**, 2469-2476 (2015)
6. S. Harisingh, S. Ramakrishnan, M. Kulbak, I. Levine, D. Cahen, B. E. Cohen, L. Etgar, M. Asscher, $CsPbBr_3$ and $CH_3NH_3PbBr_3$ promote visible-light photo-reactivity. Phys. Chem. Chem. Phys. **20**, 16847-16852 (2018)
7. T. Kinoshita, K. Nonomura, N.J. Jeon, F. Giordano, A. Abate, S. Uchida, T. Kubo, S.I. Seok, M.K. Nazeeruddin, A. Hagfeldt, Spectral splitting photovoltaics using perovskite and wideband dye-sensitized solar cells. Nat. Commun. **6**, 8834/1-8 (2015)

8. A. Zohar, M. Kulbak, I. Levine, G. Hodes, A. Kahn, D. Cahen, What limits the open-circuit voltage of bromide perovskite-based solar cells? ACS Energy Lett. **4**, 1-7 (2018)
9. O. Vybornyi, S. Yakunin, M.V. Kovalenko, Polar-solvent-free colloidal synthesis of highly luminescent alkylammonium lead halide perovskite nanocrystals. Nanoscale **8**, 6278-6283 (2016)
10. M. Saliba, T. Matsui, J. Y. Seo, K. Domanski, J.P.C. Baena, M.K. Nazeeruddin, S.M. Zakeeruddin, W. Tress, A. Abate, A. Hagfeldt, Cesium-containing triple cation perovskite solar cells: improved stability, reproducibility and high efficiency. Energy Environ. Sci. **9**, 1853-2160 (2016)
11. J. You, Z. Hong, Y. Yang, Q. Chen, M. Cai, T.B. Song, C.C. Chen, S. Lu, Y. Liu, H. Zhou, Low-temperature solution-processed perovskite solar cells with high efficiency and flexibility. ACS Nano **8**, 1674-1680 (2014)
12. A. Kojima, K. Teshima, Y. Shirai, T. Miyasaka, Organometal halide perovskites as visible- light sensitizers for photovoltaic cells. J. Am. Chem. Soc. **131**, 6050-6051 (2009)
13. K.A. Bush, A.F. Palmstrom, Z.J. Yu, M. Boccard, R. Cheacharoen, J.P. Mailoa, D.P. McMeekin, R.L.Z. Hoye, C.D. Bailie, T. Leijtens, I.M. Peters, M.C. Minichetti, N. Rolston, R. Prasanna, S. Sofia, D. Harwood, W. Ma, F. Moghadam, H.J. Snaith, T. Buonassisi, Z.C. Holman, S.F. Bent, M.D. McGehee, 23.6%-efficient monolithic perovskite/silicon tandem solar cells with improved stability. Nat. Energy **2**, 17009-17026 (2017)
14. W. Xiang, Z. Wang, D.J. Kubicki, W. Tress, J. Luo, D. Prochowicz, S. Akin, L. Emsley, J. Zhou, G. Dietler, Europium-doped $CsPbI_2Br$ for stable and highly efficient inorganic perovskite solar cells. Joule **3**, 205-214 (2018)
15. N.G. Park, Research direction toward scalable, stable, and high efficiency perovskite solar cells. Adv. Energy Mater. **10**, 1903106/1-14 (2020)
16. S. Chen, L. Lei, S. Yang, Y. Liu, Z.S. Wang, Characterization of perovskite obtained from two-step deposition on mesoporous titania. ACS Appl. Mater. Interfaces **7**, 25770-25776 (2015)
17. N.J. Jeon, J. H. Noh, Y.C. Kim, W.S. Yang, S. Ryu, S.I. Seok, Solvent engineering for high-performance inorganic-organic hybrid perovskite solar cells. Nat. Mater. **13**, 897-903 (2014)
18. N. J. Jeon, J. H. Noh, W. S. Yang, Y. C. Kim, S. Ryu, J. Seo, S. I. Seok, Compositional engineering of perovskite materials for high-performance solar cells. Nature **517**, 476-480 (2015)
19. M. Alsari, O. Bikondoa, J. Bishop, M.A. Jalebi, L.Y. Ozer, M. Hampton, P. Thompson, M.T. Hörantner, S. Mahesh, C. Greenland, In situ simultaneous photovoltaic and structural evolution of perovskite solar cells during film formation. Energ. Environ. Sci. **11**, 383-393 (2018)
20. J. Burschka, N. Pellet, S.J. Moon, R. Humphry-Baker, P. Gao, M.K. Nazeeruddin, M. Gratzel, Sequential deposition as a route to high-performance perovskite-sensitized solar cells. Nature **499**, 316-319 (2013)
21. S.S. Mali, C.S. Shim, C.K. Hong, Highly stable and efficient solid-state solar cells based on methylammonium lead bromide ($CH_3NH_3PbBr_3$) perovskite quantum dots. NPG Asia Mater. **7**, 86-95 (2015)
22. J. Avila, C. Momblona, P.P. Boix, M. Sessolo, H.J. Bolink, Vapor-deposited perovskites: the route to high-performance solar cell production. Joule **1**, 431-442 (2017)

23. X. Cao, L. Zhi, Y. Jia, Y. Li, X. Cui, K. Zhao, L. Ci, K. Ding, J. Wei, High annealing temperature induced rapid grain coarsening for efficient perovskite solar cells. J. Colloid Interface Sci. **524**, 483-489 (2018)
24. F. Fang, J. Chen, G. Wu, H. Chen, Highly efficient perovskite solar cells fabricated by simplified one-step deposition method with non-halogenated anti-solvents. Org. Electron. **59**, 330-336 (2018)
25. C. Lan, H. Lan, G. Liang, J. Zhao, H. Peng, B. Fan, Z. Zheng, H. Sun, J. Luo, P. Fan, Simultaneous formation of $CH_3NH_3PbI_3$ and electron transport layers using antisolvent method for efficient perovskite solar cells. Thin Solid Films **660**, 75-81 (2018)
26. J.W. Lee, N.G. Park, Two-step deposition method for high-efficiency perovskite solar cells. MRS Bull. **40**, 654-659 (2015)
27. Y. Tidhar, E. Edri, H. Weissman, D. Zohar, G. Hodes, D. Cahen, B. Rybtchinski, S. Kirmayer, Crystallization of methyl ammonium lead halide perovskites: implications for photovoltaic applications. J. Am. Chem. Soc. **136**, 13249-13256 (2014)
28. X. Zheng, B. Chen, C. Wu, S. Priya, Room temperature fabrication of $CH_3NH_3PbBr_3$ by anti- solvent assisted crystallization approach for perovskite solar cells with fast response and small J-V hysteresis. Nano Energy **17**, 269-278 (2015)
29. Y.C. Choi, S.W. Lee, D.H. Kim, Antisolvent-assisted powder engineering for controlled growth of hybrid $CH_3NH_3PbI_3$ perovskite thin films. APL Mater. **5**, 026101/1-6 (2017)
30. N.K. Kumawat, A. Dey, A. Kumar, S.P. Gopinathan, K. Narasimhan, D. Kabra, Band gap tuning of $CH_3NH_3Pb(Br_{1-x}Cl_x)_3$ Hybrid perovskite for blue electroluminescence. ACS Appl. Mater. Interfaces **7**, 13119-13124 (2015)
31. T. Zhang, M. Yang, E.E. Benson, Z. Li, J. van de Lagemaat, J.M. Luther, Y. Yan, K. Zhu, Y. Zhao, A facile solvothermal growth of single crystal mixed halide perovskite $CH_3NH_3Pb(Br_{1-x}Cl_x)_3$. Chem. Commun. **51**, 7820-7823 (2015)
32. S. Saeed, J. Yin, M.A. Khalid, P.A. Channar, G. Shabir, A. Saeed, M.A. Nadeem, C. Soci, A. Iqbal, Photoresponsive azobenzene ligand as an efficient electron acceptor for luminous CdTe quantum dots. J. Photochem. Photobiol. A **375**, 48-53 (2019)
33. S. Saeed, P.A. Channar, F.A. Larik, A. Saeed, M.A. Nadeem, A. Iqbal, Charge/energy transfer dynamics in CuO quantum dots attached to photoresponsive azobenzene ligand. J. Photochem. Photobiol. A **371**, 44-49 (2019)
34. S.N. Manjunatha, Y-X. Chu, M-J. Jeng, L-B. Chang, The characteristics of perovskite solar cells fabricated using DMF and DMSO/GBL solvents. J. Electron. Mater. **1**, 1-6 (2020)
35. P-H. Huang, Y-H. Wang, J-C. Ke, C-J. Huang, The effect of solvents on the performance of $CH_3NH_3PbI_3$ perovskite solar cells. Energies **10**, 599/1-8 (2017)
36. Y. Sun, J. Peng, Y. Chen, Y. Yao, Z. Liang, Triple-cation mixed-halide perovskites: towards efficient, annealing-free and air-stable solar cells enabled by Pb $(SCN)_2$ additive. Sci. Rep. **7**, 46193/1-7 (2017)
37. G.P. Nagabhushana, R. Shivaramaiah, A. Navrotsky, Direct calorimetric verification of thermodynamic instability of lead halide hybrid perovskites. Proc. Natl. Acad. Sci. **113**, 7717-7721 (2016)
38. A.K. Jena, A. Kulkarni, T. Miyasaka, Halide perovskite photovoltaics: background, status, and future prospects. Chem. Rev. **119**, 3036-3103 (2019)

39. Z. Li, M. Yang, J-S. Park, S-H. Wei, J-J. Berry, K. Zhu, Stabilizing perovskite structures by tuning tolerance factor: formation of formamidinium and cesium lead iodide solid-state alloys. Chem. Mater. **28**, 284-292 (2016)
40. W. Peng, L. Wang, B. Murali, K.T. Ho, A. Bera, N. Cho, C.F. Kang, V.M. Burlakov, J. Pan, L. Sinatra, Solution-grown monocrystalline hybrid perovskite films for hole-transporter-free solar cells. Adv. Mater. **28**, 3383-3390 (2016)
41. P. Pistor, T. Burwig, C. Brzuska, B. Weber, W. Franzel, Thermal stability and miscibility of co-evaporated methyl ammonium lead halide ($MAPbX_3$, X= I, Br, Cl) thin films analysed by in situ X-ray diffraction. J. Mater. Chem. A **6**, 11496-11506 (2018)
42. D. Priante, I. Dursun, M. Alias, D. Shi, V. Melnikov, T.K. Ng, O.F. Mohammed, O.M. Bakr, B.S. Ooi, The recombination mechanisms leading to amplified spontaneous emission at the true-green wavelength in $CH_3NH_3PbBr_3$ perovskites. Appl. Phys. Lett. **106**, 081902/1-4 (2015)
43. J.H. Noh, S.H. Im, J.H. Heo, T.N. Mandal, S.I. Seok, Chemical management for colorful, efficient, and stable inorganic–organic hybrid nanostructured solar cells. Nano Letts. **13**, 1764-1769 (2013)
44. X. Fang, K. Zhang, Y. Li, L. Yao, Y. Zhang, Y. Wang, W. Zhai, L. Tao, H. Du, G. Ran, Effect of excess $PbBr_2$ on photoluminescence spectra of $CH_3NH_3PbBr_3$ perovskite particles at room temperature. Appl. Phys. Lett. **108**, 071109/1-4 (2016)
45. M. Yang, D.H. Kim, Y Yu, Z. Li, O.G. Reid, Z. Song, D. Zhao, C. Wang, L. Li, Y. Meng, Effect of non-stoichiometric solution chemistry on improving the performance of wide-bandgap perovskite solar cells. Materials today energy **7**, 232-238 (2018)
46. C. Fei, B. Li, R. Zhang, H. Fu, J. Tian, G. Cao, Highly efficient and stable perovskite solar cells based on monolithically grained $CH_3NH_3PbI_3$ film. Adv. Energy Mater. **7**, 1602017/1-10 (2017)
47. D.H. Kim, J. Park, Z. Li, M. Yang, J-S. Park, I. J. Park, J. Y. Kim, J. J. Berry, G. Rumbles, K. Zhu, 300% enhancement of carrier mobility in uniaxial-oriented perovskite films formed by topotactic-oriented attachment. Adv. Mater. **29**, 1606831/1-8 (2017)
48. A. Mancini, P. Quadrelli, C. Milanese, M. Patrini, G. Guizzetti, L. Malavasi, $CH_3NH_3Sn_xPb_{1-x}Br_3$ hybrid perovskite solid solution: synthesis, structure, and optical properties. Inorg. Chem. **54**, 8893-8895 (2015)
49. M. Zhang, H. Yu, M. Lyu, Q. Wang, J.H. Yun, L. Wang, Composition-dependent photoluminescence intensity and prolonged recombination lifetime of perovskite $CH_3NH_3PbBr_{3-x}Cl_x$ films. Chem. Commun. **50**, 11727-11730 (2014)
50. M.B. Johnston, L.M. Herz, Hybrid perovskites for photovoltaics: charge-carrier recombination, diffusion, and radiative efficiencies. Acc. Chem. Res. 49, 146-154 (2016)
51. S. Saeed, A. Iqbal, A. Iqbal, Photoinduced charge carrier dynamics in a ZnSe quantum dot- attached CdTe system. Proc. R. Soc. A **476**, 20190616/1-13 (2020)
52. J. Hao, H. Hao, J. Li, L. Shi, T. Zhong, C. Zhang, J. Dong, J. Xing, H. Liu, Z. Zhang, Light trapping effect in perovskite solar cells by the addition of Ag nanoparticles, using textured substrates. Nanomater. **8**, 815/1-12 (2018)
53. J.W. Lee, Z. Dai, T.H. Han, C. Choi, S.Y. Chang, S.J. Lee, N. De Marco, H. Zhao, P. Sun, Y. Huang, 2D perovskite stabilized phase-pure formamidinium perovskite solar cells. Nat. Commun. **9**, 3021/1-10 (2018)

54. M.I. Saidaminov, M.A. Haque, J. Almutlaq, S. Sarmah, X.H. Miao, R. Begum, A.A. Zhumekenov, I. Dursun, N. Cho, B. Murali, Inorganic lead halide perovskite single crystals: phase-selective low-temperature growth, carrier transport properties, and self-powered photodetection. Adv. Opt. Mater. **5**, 1600704-1600711 (2017)
55. J. Deng, J. Xun, R. He, Facile and rapid synthesis of high performance perovskite nanocrystals CsPb $(X/Br)_3$ (X= Cl, I) at room temperature. Opt. Mater. **99**, 109528/1-6 (2020)
56. Z. Yuan, Y. Shu, Y. Xin, B. Ma, Highly luminescent nanoscale quasi-2D layered lead bromide perovskites with tunable emissions. Chem. Commun. **52**, 3887-3890 (2016)
57. A. Dualeh, P. Gao, S.I. Seok, M.K. Nazeeruddin, M. Graatzel, Thermal behavior of methylammonium lead-trihalide perovskite photovoltaic light harvesters. Chem. Mater. **26**, 6160-6164 (2014)
58. H. Mehdi, A. Mhamdi, R. Hannachi, A. Bouazizi, $MAPbBr_3$ perovskite solar cells via a two- step deposition process. RSC Adv. **9**, 12906-12912 (2019)
59. T.D. McFarlane, C.S.D. Castro, P.J. Holliman, M.L. Davies, Improving the light harvesting and colour range of methyl ammonium lead tri-bromide ($MAPbBr_3$) perovskite solar cells through co-sensitisation with organic dyes, Chem. Commun. **55**, 35-38 (2019)
60. X. Hu, X.F. Jiang, X. Xing, L. Nian, X. Liu, R. Huang, K. Wang, H.L. Yip, G. Zhou, Wide-bandgap perovskite solar cells with large open-circuit voltage of 1653 mv through interfacial engineering. Solar RRL **2**, 1800083/1-10 (2018)
61. T. Kokab, Z. Siddique, S. Hussain, A. Iqbal, Doped quaternary metal chalcogenides Cu_2ZnSnS_4 nanocrystals as efficient light harvesters for solar cell devices. J. Mater. Sci.: Mater. Electron. **30**, 20860-20869 (2019)
62. H. Zhou, Q. Chen, G. Li, S. Luo, T-B. Song, H-S. Duan, Z. Hong, J. You, Y. Liu, Y. Yang, Interface engineering of highly efficient perovskite solar cells. Science **345**, 542-546 (2014)
63. K. Gao, Z. Zhu, B. Xu, S.B. Jo, Y. Kan, X. Peng, A. K-Y. Jen, Highly efficient porphyrin-based OPV/perovskite hybrid solar cells with extended photoresponse and high fill factor. Adv. Mater. **29**, 1703980/1-8 (2017)
64. K. Gao, J. Miao, L. Xiao, W. Deng, Y. Kan, T. Liang, C. Wang, F. Huang, J. Peng, Y. Cao, Multi-length-scale morphologies driven by mixed additives in porphyrin-based organic photovoltaics. Adv. Mater. **28**, 4727-4733 (2016)
65. K. Gao, Y. Kan, X. Chen, F. Liu, B. Kan, L. Nian, X. Wan, Y. Chen, X. Peng, T.P. Russell, Low-Bandgap Porphyrins for Highly Efficient Organic Solar Cells: Materials, Morphology, and Applications. Adv. Mater. **32**, 1906129/1-19 (2020)
66. K. Gao, S. B. Jo, X. Shi, L. Nian, M. Zhang, Y. Kan, F. Lin, B. Kan, B. Xu, Q. Rong, Over 12% efficiency nonfullerene all-small-molecule organic solar cells with sequentially evolved multilength scale morphologies, Adv. Mater. **31**, 1807842/1-10 (2019)
67. D. Liu, C. Yang, Lunt, R.R. Halide perovskites for selective ultraviolet-harvesting transparent photovoltaics. Joule **2**, 1827-1837 (2018)